Mesoscopic Cohesive Crack Model of Microcapsule Self-Healing Concrete and Its Uniaxial and Triaxial Compression Simulation

Yuhong Liu, Jierong Liang, Xianfeng Wang*, Dawei Qin and Weilun Wang

Guangdong Provincial Key Laboratory of Durability for Marine Civil Engineering, College of Civil and Transportation Engineering, Shenzhen University, Shenzhen, Guangdong 518060, China

Abstract: In practical engineering structures, concrete is usually under a multiaxial stress state. Therefore, it is significant to investigate the mechanical behavior of microcapsule self-healing concrete under triaxial compression. In this study, a three-dimensional mesoscopic cohesive crack model of concrete based on the cohesive element is established to simulate uniaxial compression tests and conventional triaxial tests of concrete with different microcapsule content. The result shows that when the uniaxial compressive loading reaches $\sigma = 0.4\sigma_{\max}$, a small number of microcracks start to appear, leading to the nonlinear behavior of the stress-strain curve. When the uniaxial compression is loaded near the peak point ($\sigma = 0.9{\sim}1.0\sigma_{\max}$), the internal cracks of the sample begin to increase sharply. Different from the crack of the sample in uniaxial compression concentrated in the interfacial transition zone, the crack of the sample in triaxial compression is scattered in the interior of the mortar and the interfacial transition zone, and the greater the confining pressure, the more crack in the mortar.

Keywords: Concrete, Triaxial compression, Cohesive crack model, Cohesive element, Random aggregate model, Mesoscopic fracture.

1. INTRODUCTION

Concrete material has the advantages of superior mechanical properties, relatively low cost, and strong plasticity, hence is one of the most widely used materials in the construction industry [1]. However, concrete materials almost inevitably develop cracks in service [2]. Therefore, scholars have proposed the concept of self-healing concrete [3-4], that is, by embedding artificial functional materials in concrete to realize the self-healing of concrete cracks to prolong the service life of concrete structures.

The mechanical behavior of self-healing concrete is one of the current research focuses. On the mesoscale, cracking is a common phenomenon of concrete failure. With the development of computer technology and the maturity of finite element analysis methods, it is possible to study the multiaxial mechanical properties of concrete from the mesoscopic scale. In recent years, researchers have proposed a variety of concrete micro-crack models, which can usually be divided into three types: continuous, discrete, and mixed [5]. Among them, the hybrid crack model with cohesive element embedded on the boundary of conventional finite element elements can realize the displacement discontinuity caused by node separation during loading. This method can reflect the initiation and expansion process of microcracks in concrete, so it has been widely used in the simulation research of concrete cracking [6-8]. Zhang *et al*. [9] used a two-dimensional cohesive crack model to simulate the uniaxial tension process of concrete with deformed aggregates, and found that the probability of deformed aggregate breakage increases with the increase in the proportion of deformed aggregates. Yang *et al*. [10] simulated the uniaxial tensile process and crack development process of concrete by establishing a cohesive crack model of random three-dimensional polyhedral aggregates, and found that the mechanical behavior of concrete depends on both fracture material parameters and aggregate shape parameters. Liu [11] simulated the uniaxial compression and tension process of asphalt concrete by establishing a three-dimensional cohesive crack model, and obtained the crack development characteristics and fracture surface shape of the asphalt concrete failure process. However, the current research models mainly use two-dimensional or relatively simple aggregate shapes, and the loading methods mainly use uniaxial tension and uniaxial compression. There are relatively few studies on random 3D polygonal aggregate models and triaxial compression loads.

The triaxial mechanical behavior is an important performance index of concrete. Deng *et al*. [12] conducted a triaxial compression test of recycled aggregate concrete under high temperature, and found that the true triaxial compressive strength and peak strain of concrete under high temperature conditions were greater than the uniaxial compressive strength and peak strain at room temperature. Su *et al*. [13] conducted a series of uniaxial and triaxial tests on foamed concrete and found that foamed concrete exhibits brittle failure under uniaxial compression, and the confining pressure level can significantly improve the mechanical properties of concrete under triaxial loading. Mo [14] conducted a triaxial compression test

Address correspondence to this article at the College of Civil and Transportation Engineering, Shenzhen University, Shenzhen, Guangdong 518060, China; Tel: +86 755 2673 2843;
E-mail: xfw@szu.edu.cn

E-ISSN: 2409-9848/23

on ordinary concrete cube specimens with three sizes of 100mm, 150mm, and 200mm respectively. The result shows that the peak strength and peak strain of the specimens under triaxial compression have a size effect that decreases with the increase of the stress ratio. Therefore, it is necessary to explore the triaxial mechanical behavior of self-healing concrete.

In this paper, from the perspective of numerical simulation, a three-dimensional mesoscopic cohesive crack model of microcapsule self-healing concrete based on the cohesive element is established. The influence of different material parameters on the mechanical properties of concrete is analyzed. The material parameters of three kinds of concrete under different working conditions are determined. Uniaxial and triaxial compression tests of three types of concrete are simulated. The damage and fracture process of concrete under various working conditions is discussed.

2. METHOD

2.1. Geometric Modeling

Firstly, a mesoscopic model without cohesive element is established. This process includes two steps of aggregate generation and aggregate placement [11]. Aggregate generation can obtain polyhedron aggregate by random growth or adjustment point method. Then the aggregate is placed in the sample space without overlapping to achieve the aggregate placement. In this study, the POLARIS_MesoConcrete plug-in of the finite element software ABAQUS is used to generate the mesoscopic model. As shown in Figure **1**, the cubic random aggregate model with a size of 100 mm × 100 mm × 100 mm is generated. The volume of aggregate with the particle size of 5.0-10.0 mm, 10.0-16.0 mm, and 16.0-20.0 mm accounted for 6%, 11%, and 15% of the specimen volume, respectively. Then, the cubic geometry model is meshed in ABAQUS to a continuous model (the mesh size is up to 3 mm).

Secondly, to generate the cohesive crack model, the zero-thickness cohesive element is embedded between the aggregate element and the mortar element, and between adjacent elements inside the mortar material. This process is based on element mesh topology and requires the insertion of cohesive element with appropriate numbered order between the elements of the continue model, which has been achieved in our previous study [11]. As shown in Figure **2**, the model is composed of the coarse aggregate element, the mortar element, the aggregate-mortar interface cohesive element, and the mortar internal cohesive element.

2.2. Material Constitutive Relations

In the concrete mesoscopic model, the elements corresponding to the coarse aggregate and mortar components are assumed to be linear elasticity, while the cohesive elements corresponding to the

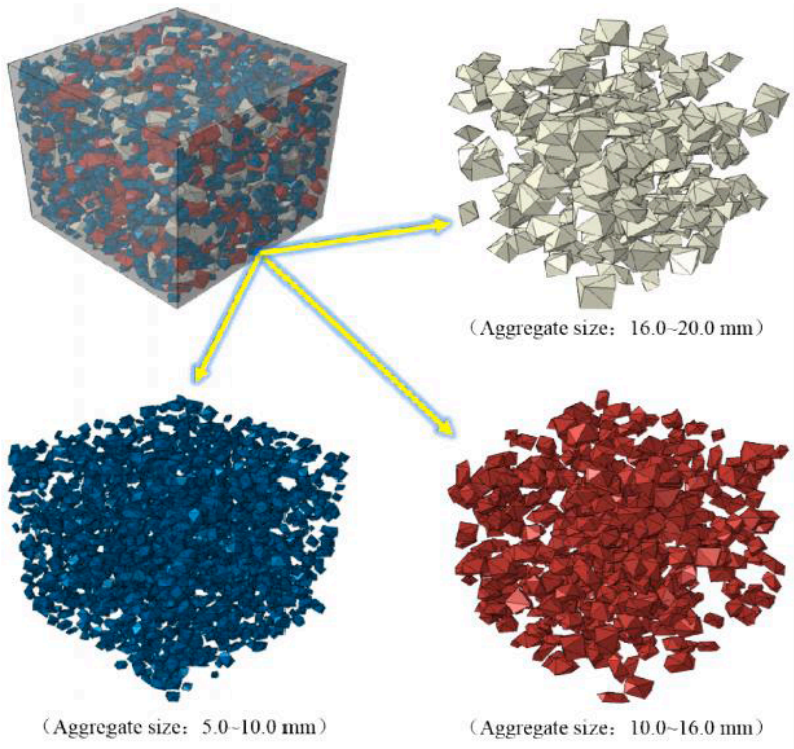

Figure 1: Random aggregate placement.

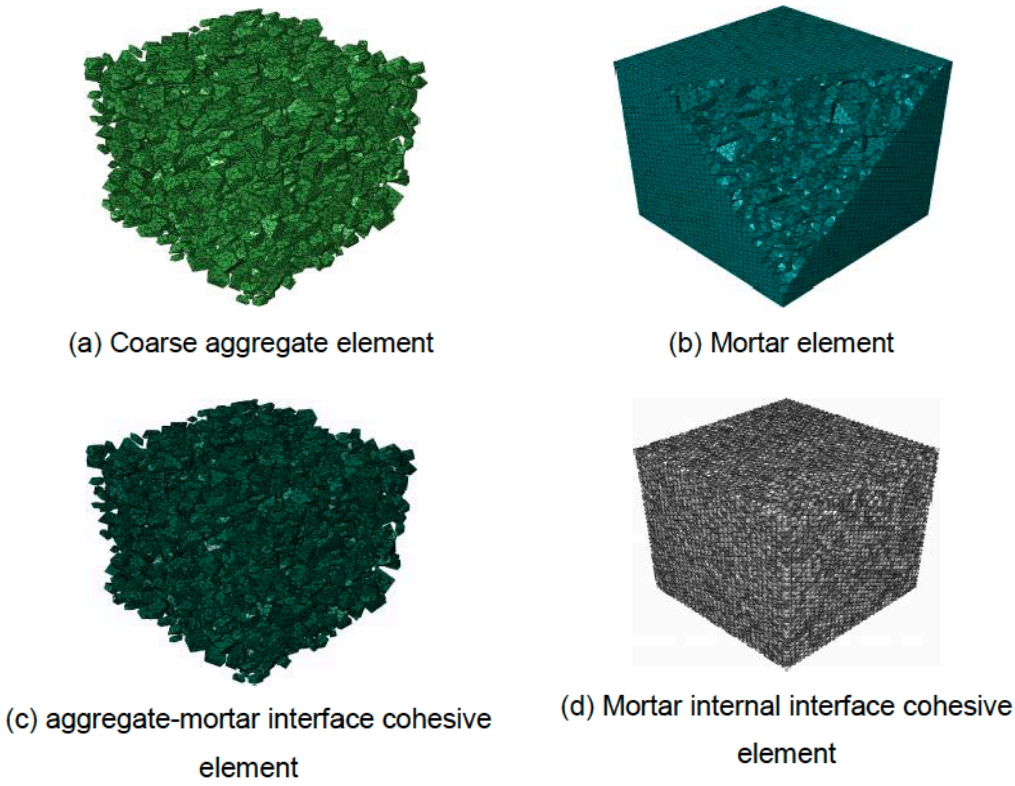

(a) Coarse aggregate element

(b) Mortar element

(c) aggregate-mortar interface cohesive element

(d) Mortar internal interface cohesive element

Figure 2: Model element composition.

aggregate-mortar interface and the internal interface of the mortar adopt a bilinear traction-separation relationship. As shown in Figure **3**, the bilinear traction-separation relationship of the cohesive element includes the elastic stage, damage stage, and failure stage. 1) Elastic stage: the separation displacement is smaller than the initial damage displacement, hence the traction of the cohesive element increases linearly with the increase of the separation displacement at this stage; 2) Damage stage: the separation displacement is between the initial damage displacement and the failure displacement, hence the cohesive element begins to be damaged, and the stiffness and maximum traction of the cohesive element begin to decay; 3) Failure stage: the separation displacement is greater than the failure displacement, hence the cohesive element fails and loses its bearing capacity. It is worth noting that the normal relationship of cohesive element expresses the stretch and compression behavior of concrete. Therefore, the normal stretching behavior is considered to conform to the above relationship, while the normal compression behavior is considered to be linear elasticity without damage.

In Abaqus, the damage evolution equation of cohesive element can be expressed as:

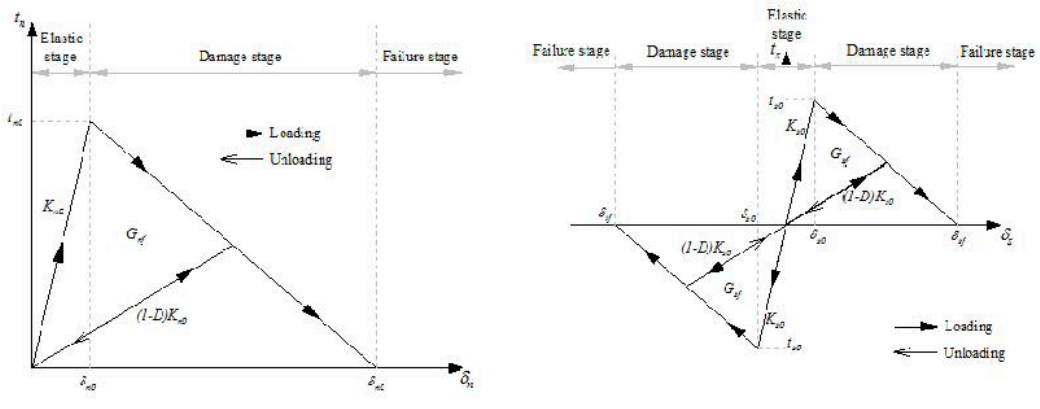

(a) Normal relationship

(b) Tangential relationship

Figure 3: Bond element constitutive relation.

$$D = \frac{\delta_m^f(\delta_m^{max}-\delta_m^0)}{\delta_m^{max}(\delta_m^f-\delta_m^0)} \quad (1)$$

$$\delta_m = \sqrt{\langle\delta_n\rangle^2 + {\delta_s}^2} \quad (2)$$

where D is the damage variable, δ_m is the effective displacement, $\langle\ \rangle$ is the Macaulay symbol, δ_m^0 is the effective displacement at the initial damage, δ_m^f is the effective displacement at failure, and δ_m^{max} is the maximum effective displacement in the loading history.

Since the separation displacement of cohesive element is difficult to measure, it is usually expressed by the fracture energy as shown below.

$$\delta_f = 2G_f/t_0 \quad (3)$$

where δ_f is the failure displacement, G_f is the fracture energy, and t_0 is the peak strength.

The stiffness and traction of cohesive element after damage can be expressed as:

$$K_n = (1-D)K_{n0} \quad (4)$$

$$K_s = (1-D)K_{s0} \quad (5)$$

$$t_n = \begin{cases}(1-D)\overline{t_n}\ ,\ \overline{t_n} \geq 0\\ \overline{t_n}\ ,\ \overline{t_n} < 0\end{cases} \quad (6)$$

$$t_s = (1-D)\overline{t_s} \quad (7)$$

where $\overline{t_n}$ and $\overline{t_s}$ are the normal and tangential traction corresponding to the current separation displacement under the undamaged state, respectively.

The damage initiation criterion can be expressed as:

$$\left\{\frac{\langle t_n\rangle}{t_{n0}}\right\}^2 + \left\{\frac{t_s}{t_{s0}}\right\}^2 = 1 \quad (8)$$

where t_n and t_s are the normal and tangential strengths, respectively, and t_{n0} and t_{s0} are the peak values of the normal and tangential strengths, respectively.

2.3. Material Parameters

Based on the research of scholars [6,10,15], the basic material parameters can be obtained, as shown in Table **1**. However, most of the previous studies focus on the uniaxial tension simulation of concrete, and the calibrated material parameters were usually applied in the uniaxial tension conditions. Liu [16] simulates the uniaxial compression of concrete based on the material parameters shown in Table **1**. The result shows that: under compression, the deformation of the cohesive element is mainly shear, and the failure of the specimen is dominated by shear damage. Therefore, it is necessary to continuously adjust the tangential bond strength (t_{s0}) to ensure that the simulation result is consistent with the experimental result. In addition, Xu *et al*. [17] believes that compared with mode I fracture energy, the mode II shear fracture energy is more suitable for compression conditions. Therefore, among the model material parameters in this chapter, the tangential cohesive strength and fracture energy of cohesive elements are undetermined parameters, which will be analyzed in subsequent chapters and calibrated according to the test result.

3. RESULTS AND DISCUSSION

3.1. Uniaxial Compression Simulation

3.1.1. Model Settings and Material Parameter Sensitivity Analysis

In the uniaxial compression simulation, the Abaqus/Explicit product is used for quasi-static analysis [11]. Apply vertical displacement constraint to all nodes at the bottom of the specimen, and apply lateral displacement constraint to the central node at the bottom. Then a vertical compression displacement of 0.5 mm is applied to all nodes on the top of the specimen.

To explore the influence of parameters such as tangential bond strength, fracture energy, and stiffness on the uniaxial compression simulation result, this

Table 1: Material Parameters [15]

Components	Young modulus *E* (MPa)	Poisson ratio υ	Density ρ (10^{-9} t/mm^3)	Rigidity K (10^6 MPa/mm)	Normal bonding strength t_{n0} (MPa)	Tangential bond strength t_{s0} (MPa)	Fracture energy G_f (N/mm)
Aggregate	70000	0.2	2.5	/	/	/	/
Mortar	25000	0.2	2.2	/	/	/	/
Aggregate-mortar interface	/	/	2.2	1	3	*Ti* (variable)	*Gi* (variable)
Mortar internal interface	/	/	2.2	1	6	*Tc* (variable)	*Gc* (variable)

paper sets up the following different working groups according to the principle of control variables. As shown in Table **2**, keeping the fracture energy (Gc=0.3, Gi=0.15) and other material parameters (see Table **1**) constant, different tangential bond strengths are taken for the cohesive element. The tangential bond strength of the cohesive element is half of that of the mortar cohesive element. Using the TcTi numbering rule, such as the number Tc6Ti3, indicates that the tangential bond strength of the mortar cohesive element and interface cohesive element are 6MPa and 3MPa, respectively. As shown in Table **3**, keep the tangential bond strength (Tc=15, Ti=7.5) constant, other material parameters (see Table 1) constant, and take different fracture energy for the cohesive element. The fracture energy of the cohesive element is half of that of the mortar cohesive element. Using the GcGi numbering rule, for example, the number Gc0.30Gi0.15 indicates that the fracture energy of the mortar cohesive element and the interface cohesive element are 0.3 N/mm and 0.15 N/mm, respectively. As shown in Table **4**, keeping other parameters (see Table **1**) unchanged, the stiffness of the cohesive element, and the elastic modulus of the aggregate and mortar element are taken as different values. Using the KEsEc numbering rule, such as the number K5Es70Ec25, indicates that the stiffness of the cohesive element is 105 MPa/mm, and the elastic modulus of the aggregate and mortar element are 70 GPa and 75 GPa, respectively.

Table 2: Groups Setting of Different Tangential Bond Strength Parameters

Number	Tangential bond strength t_{s0} (MPa)	
	Mortar internal (Tc)	Aggregate-mortar interface (Ti)
Tc6Ti3	6	3
Tc15Ti7.5	15	7.5
Tc30Ti15	30	15
Tc60Ti30	60	30
Tc120Ti60	120	60

Table 3: Groups Setting of Different Fracture Energy Parameters

Number	Fracture energy G_f (N/mm)	
	Mortar internal (Gc)	Aggregate-mortar interface (Gi)
Gc0.06Gi0.03	0.06	0.03
Gc0.12Gi0.06	0.12	0.06
Gc0.30Gi0.15	0.30	0.15
Gc0.60Gi0.30	0.60	0.30
Gc0.90Gi0.45	0.90	0.45
Gc1.80Gi0.90	1.80	0.90

The effect of tangential bond strength on the stress-strain curve, peak strength and peak strain of uniaxial compression is shown in Figure **4** and Figure **5**. The effect of fracture energy on the stress-strain curve, peak strength and peak strain of uniaxial compression is shown in Figure **6** and Figure **7**. Comparing Figure **4** and Figure **6**, it can be found that the direction of the softening section after the peak of the uniaxial compressive stress-strain curve depends on the relative relationship between the tangential bond strength and the fracture energy of the cohesive element. Since the fracture energy of the curves in the figure does not change, only the tangential bond strength increases. Therefore, taking the ratio of tangential bond strength and fracture energy as an index, the larger the ratio of tangential bond strength to fracture energy, the curve will drop sharply in the post-peak section, otherwise, the curve will drop slowly in the post-peak section. It is worth noting that the tangential bond strength and fracture energy have no effect on the initial slope of the curve. In addition, observing Figure **5** and Figure **7**, it can be found that with the increase of tangential bond strength or fracture energy, the peak strength and peak strain of concrete both increase continuously and present a law that rises sharply and then tends to be gentle. In particular, comparing Tc6Ti3 and Tc60Ti30, it can be found that when the tangential bond strength increases to 10 times, the peak strength and peak strain of the concrete increase to 3.1 and 2.0 times, respectively.

Table 4: Groups Setting of Different Stiffness Parameters

Number	Cohesive element K (MPa/mm)	Aggregate element *E* (MPa)	Mortar element *E* (MPa)	Other parameters
K6Es70Ec25	10^6	70000	25000	Bond strength: Tc15Ti7.5 Fracture energy: Gc0.90Gi0.45
K6Es50Ec25	10^6	50000	25000	
K6Es50Ec22	10^6	50000	22000	
K5Es70Ec25	10^5	70000	25000	

Comparing Gc0.06Gi0.03 and Gc0.60Gi0.30, it can be found that when the fracture energy increases to 10 times, the peak strength and peak strain of concrete increase to 1.4 times and 2.0 times, respectively. This shows that the improvement of concrete strength mainly depends on the tangential bond strength, while the deformation capacity mainly depends on the fracture energy.

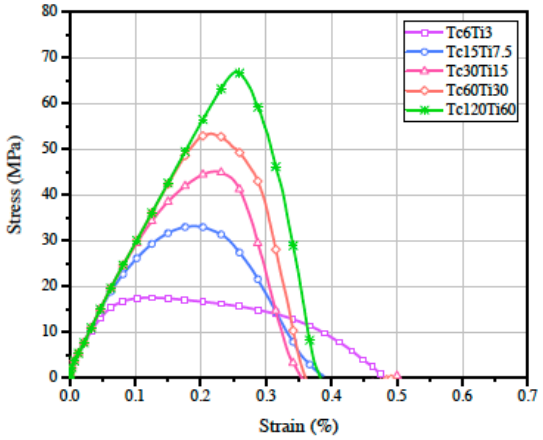

Figure 4: Influence of tangential bond strength on stress-strain curve.

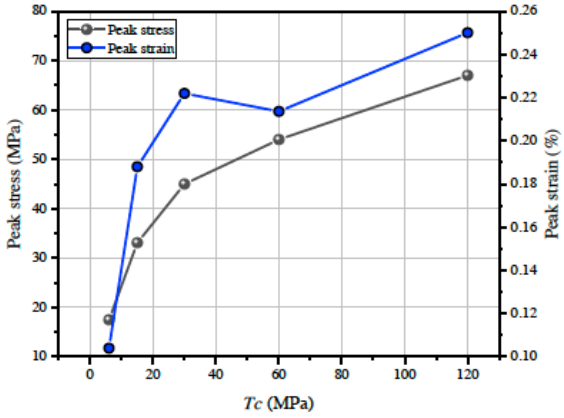

Figure 5: Effect of tangential bond strength on peak stress and peak strain.

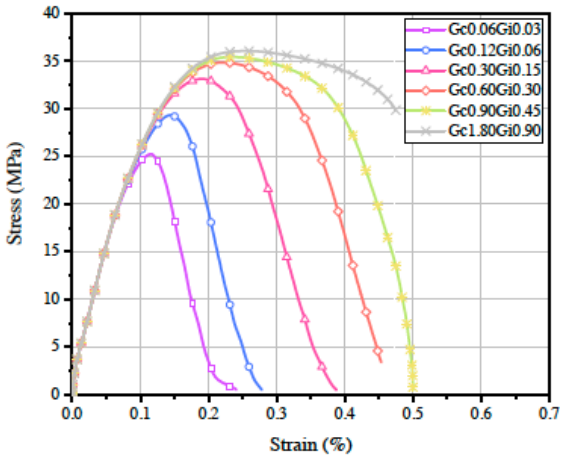

Figure 6: Influence of fracture energy on stress-strain curve.

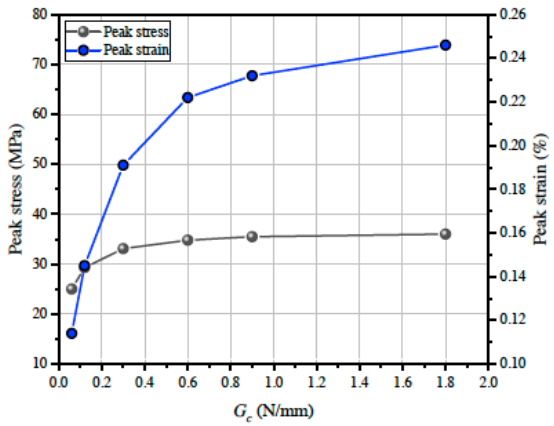

Figure 7: Effect of fracture energy on peak stress and peak strain.

The effect of different stiffness parameters on the stress-strain curve of uniaxial compression is shown in Figure **8**. It can be seen that reducing the stiffness of the cohesive element, the elastic modulus of the aggregate element, or the elastic modulus of the mortar element will lead to a decrease in the slope of the stress-strain curve. Among them, the stiffness of the cohesive element has the most significant influence on the slope of the curve. In addition, neither the stiffness of the cohesive element nor the modulus of elasticity of the aggregate and mortar element have a significant effect on the peak strength and peak strain of the concrete.

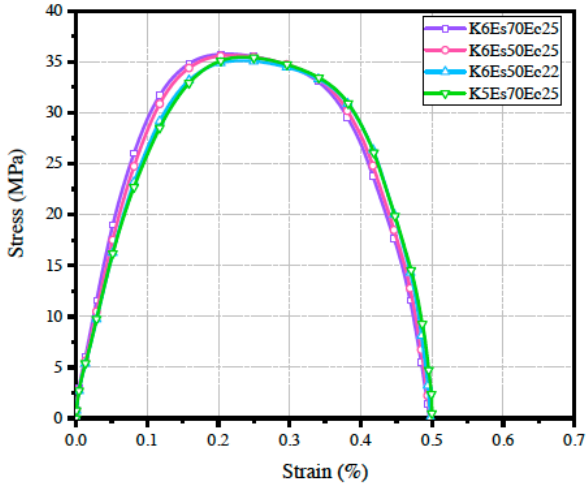

Figure 8: Influence of stiffness parameters on stress-strain curves.

3.1.2. Material Parameter Calibration

The models are built based on the three concretes C40M0, C40M3, and C40M6 (The mass ratios of microcapsules and cement are 0%, 3%, and 6%, respectively) from our previous experimental study [18-19]. Except for the number of microcapsules, the three kinds of concrete have the same mix ratio, and the microcapsules mainly affect the bond strength between the mortar and interfacial transition zone.

Therefore, for the models established for the three types of concrete, except for the tangential bond strength parameter and fracture energy parameter of the mortar internal cohesive element and the interface cohesive element, the other model material parameters are consistent. According to the conclusion of the sensitivity analysis in the previous section, the tangential bond strength parameter and fracture energy parameter of the cohesive element is adjusted in a targeted manner so that the simulation result is consistent with the result of the uniaxial compression test, thus obtaining the material parameters of the three concrete models (As shown in Table **5**). The tangential bond strength and fracture energy of different types of concrete are shown in Figure **9**. It can be seen that with the increase of the content of microcapsules in concrete, the tangential bond strength gradually decreases and the fracture energy gradually increases.

3.1.3. Uniaxial Compression Simulation Results

Figure **10** compares the simulated and experimental results of the stress-strain curves of the three concretes in uniaxial compression. It can be seen that the simulated stress-strain curve can also be divided into three stages: linear stage, elastic-plastic stage, and softening stage. For the linear stage and the elastic-plastic stage of the stress-strain curve, the simulated curve almost coincides with the experimental curve. That is, the simulation results of the peak strength, peak strain, and elastic modulus of concrete are consistent with the test result, indicating that the established model can effectively simulate the concrete

Table 5: Material Parameters of Three Concrete Models in Uniaxial Compression Simulation

Concrete type	Components	Young modulus E (MPa)	Poisson ratio υ	Density ρ (10^{-9} t/mm^3)	Rigidity K (10^6 MPa/mm)	Normal bonding strength t_{n0} (MPa)	Tangential bond strength t_{s0} (MPa)	Fracture energy G_f (N/mm)
C40M0	Aggregate	70000	0.2	2.5	/	/	/	/
	Mortar	25000	0.2	2.2	/	/	/	/
	Aggregate-mortar interface	/	/	2.2	0.1	3	8.3	0.12
	Mortar internal interface	/	/	2.2	0.1	6	16.6	0.24
C40M3	Aggregate	70000	0.2	2.5	/	/	/	/
	Mortar	25000	0.2	2.2	/	/	/	/
	Aggregate-mortar interface	/	/	2.2	0.05	3	7.1	0.15
	Mortar internal interface	/	/	2.2	0.05	6	14.2	0.30
C40M6	Aggregate	70000	0.2	2.5	/	/	/	/
	Mortar	25000	0.2	2.2	/	/	/	/
	Aggregate-mortar interface	/	/	2.2	0.04	3	6.5	0.20
	Mortar internal interface	/	/	2.2	0.04	6	13.0	0.40

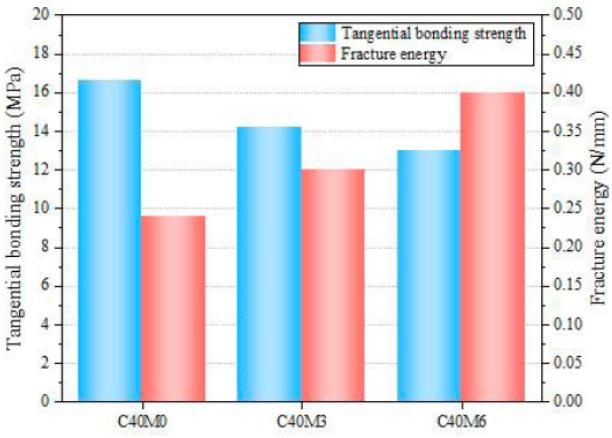

Figure 9: Tangential bond strength and fracture energy of different types of concrete.

uniaxial compression test. It is worth noting that the simulation curve drops rapidly after the peak point, which is different from the descending section of the test curve. This is caused by the rapid expansion of crack after the complete failure of some cohesive element, and the loss of quasi-static conditions in the simulation process. The descending section of the uniaxial compression simulation curve using the two-dimensional cohesive model in the research [16] is also this feature.

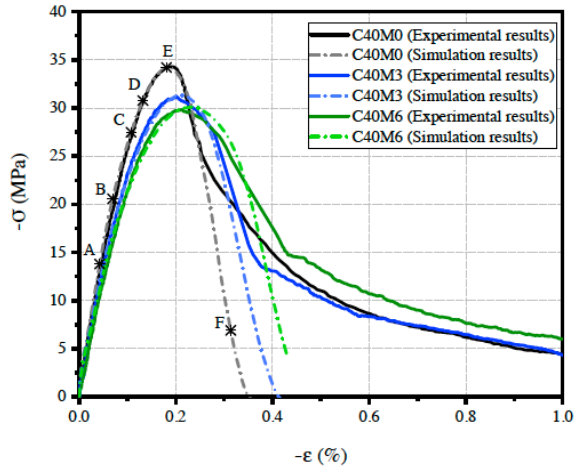

Figure 10: Comparison of simulation result and experimental result of uniaxial compression stress-strain curve.

In the uniaxial compression simulation, the failure mode of the lateral and loading surface of the model are shown in Figure **11** and Figure **12**, respectively. As shown in Figure **11**, there are relatively obvious longitudinal cracks passing through the middle of the model on the sides of the three concrete models. In addition, the loading surface of the model is divided into multiple parts by cracks (as shown in Figure **12**). This is because the model is split into separate "short column groups" [20] due to the transverse tensile strain generated by Poisson's ratio during the uniaxial compression process. Comparing Figure **11** and Figure **13**(**a**), Figure **12** and Figure **13**(**b**) can be found that whether observed from the side or the loading surface, the failure mode of the model in the simulated uniaxial compression is relatively close to that of the actual concrete specimen in the uniaxial compression test with the measure of removing the constraint of the loading plate. In addition, there is no significant difference in the failure mode between different types of concrete, which is also the same as the experimental conclusion of this paper. Therefore, the model established in this chapter can better simulate the failure mode of concrete in the uniaxial compression test.

In this paper, the formation and propagation process of the mesoscopic crack inside the sample model is analyzed by the appear and increase process of the damaged element. As shown in Figure **14**, taking the C40M0 model as an example, it shows the fracture process of the model in the uniaxial compression simulation (Figure **14**(**a**)~(**f**) corresponds to points A~F in Figure **10**, respectively). Among them, Figure **14**(**a**)~(**c**) shows the cohesive element with damage variable D≥0.9. It can be seen that when the uniaxial compression is loaded to $\sigma = 0.4\sigma_{\max}$, a small number

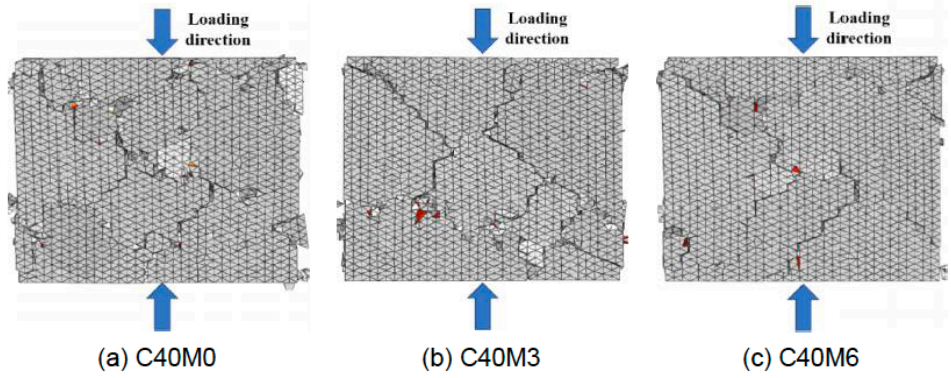

Figure 11: Failure mode of model side in uniaxial compression simulation.

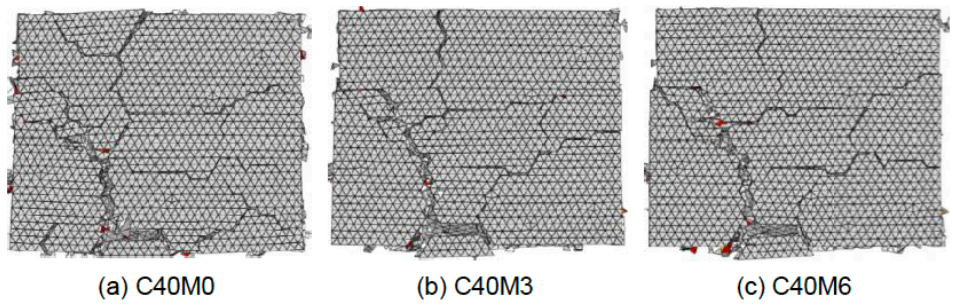

Figure 12: Failure mode of model loading surface in uniaxial compression simulation.

(a) lateral surface (b) loading surface

Figure 13: Failure mode of concrete under uniaxial compression experiment.

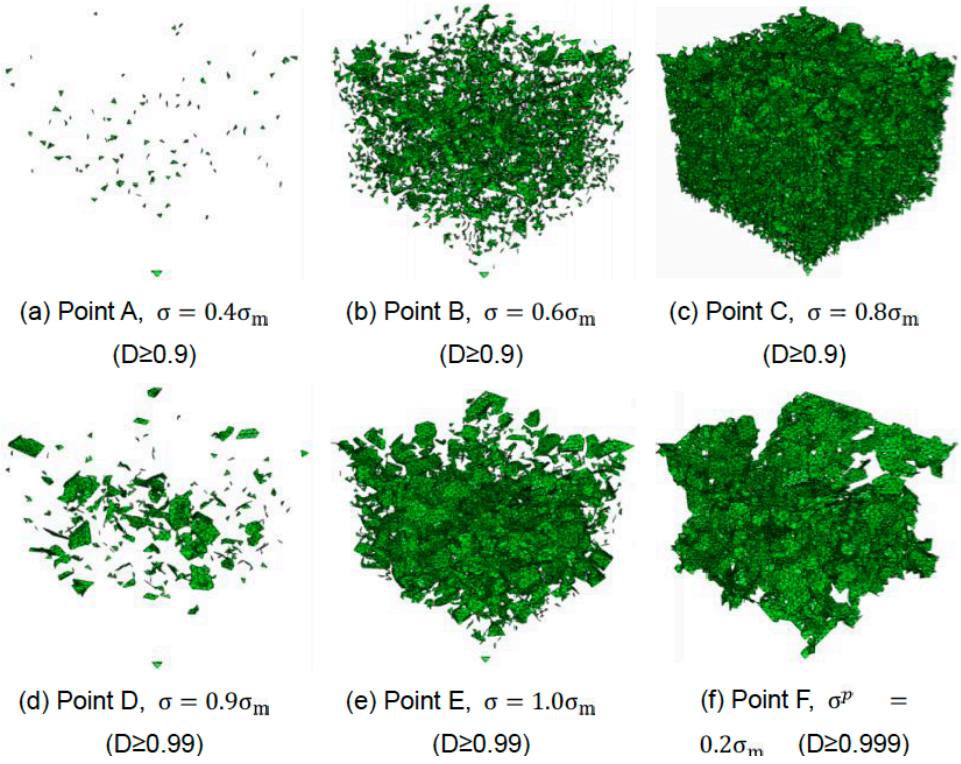

(a) Point A, $\sigma = 0.4\sigma_m$ (D≥0.9) (b) Point B, $\sigma = 0.6\sigma_m$ (D≥0.9) (c) Point C, $\sigma = 0.8\sigma_m$ (D≥0.9)

(d) Point D, $\sigma = 0.9\sigma_m$ (D≥0.99) (e) Point E, $\sigma = 1.0\sigma_m$ (D≥0.99) (f) Point F, $\sigma^p = 0.2\sigma_m$ (D≥0.999)

Figure 14: Fracture process of C40M0 model in uniaxial compression simulation (σ_{max} is the peak stress).

of the damaged element with D≥0.9 begin to appear. This type of damage element can be considered as a microcrack that causes the nonlinear behavior of the uniaxial compressive stress-strain curve because it is generally considered in the literature that $0.4\sigma_{max}$ is the dividing point between the elastic and inelastic stage of the stress-strain curve [21]. During the loading process from $\sigma = 0.4\sigma_{max}$ to $\sigma = 0.8\sigma_{max}$, the damage element with D≥0.9 increases continuously. When the uniaxial compression is loaded to $\sigma = 0.8\sigma_{max}$, most of the aggregate-mortar interface cohesive elements and mortar internal cohesive elements are damaged. This shows that concrete will produce a large number of microcracks in the elastoplastic stage of uniaxial compression. Figure **14**(**d**)~(**e**) shows the cohesive element with damage variable D≥0.99. It can be seen that when the uniaxial compression is loaded to $\sigma = 0.9\sigma_{max}$, a small number of the damaged element with D≥0.99 begin to appear, and such damaged elements can be considered as elements that form cracks [11]. When the uniaxial compression is loaded near the peak point ($\sigma = 0.9\sim1.0\sigma_{max}$), the internal cracks of the sample model begin to increase sharply, and the cracks are concentrated in the transition zone of the aggregate-mortar interface. As the loading continues, the cracks develop into the macroscopic crack and the specimen begins to fail. As shown in Figure **14**(**f**), the distribution of cohesive element with D≥0.999 is consistent with the macroscopic cracks seen on the surface of the sample, and this type of damaged element can be considered as an element representing macroscopic cracks.

3.2. Triaxial Compression Simulation

3.2.1. Model Settings and Material Parameter Calibration

As shown in Figure **15**, apply displacement constraint in the x, y, and z directions to all nodes on the three surfaces of the x, y, and z axes, and then load in two steps. The first step is to apply hydrostatic pressure to the predetermined confining pressure on the three faces of the model in the x, y, and z axes. The second step keeps the confining pressure constant and applies a vertical compression displacement of about 1 mm to all nodes on the top of the specimen.

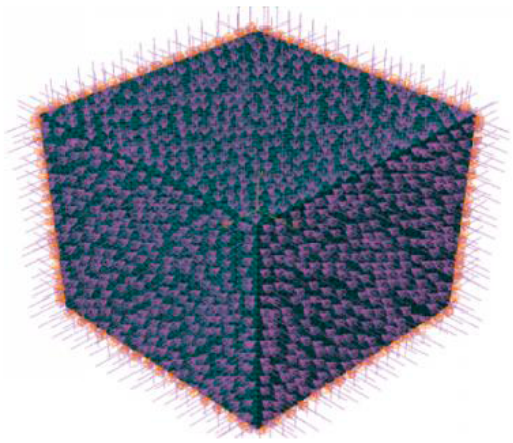

Figure 15: Triaxial compression loading mode.

Since the bilinear constitutive relation adopted by the cohesive element does not consider the influence of the confining pressure, this section recalibrates the material parameters of the cohesive element according to the triaxial test results, and explores the influence of the confining pressure on the material parameters of the cohesive element. According to relevant literature reports [22], the triaxial compressive strength of concrete can be divided into bond strength (a constant) and internal friction strength (increases with the increase of confining pressure). In addition, the confining pressure can significantly improve the deformation capacity of concrete. Therefore, this section keeps the other material parameters of the three concrete models unchanged (as shown in Table **6**), and adjusts the tangential bond strength related to the internal friction strength of the sample and the fracture energy related to the deformation capacity of the sample. Make sure that the peak stress and peak strain of the simulated triaxial compressive stress-strain curve are the same as the experimental results.

The peak stress of triaxial compression adopts the experimental result of our previous study [18-19]. Since the strain data of the triaxial test is obtained by calculating the displacement at both ends of the specimen recorded by the testing machine, it cannot accurately represent the strain of the concrete

Table 6: Tangential Bond Strength and Fracture Energy of Models in Triaxial Compression Simulation

Concrete type	Confining pressure f_l (MPa)	Components	t_{s0} (MPa)	G_f (N/mm)
C40M0	10	Aggregate-mortar interface	20.0	0.9
		Mortar internal interface	40.0	1.8
	20	Aggregate-mortar interface	25.5	1.5
		Mortar internal interface	51.0	3.0
	30	Aggregate-mortar interface	38.5	2.1
		Mortar internal interface	77.0	4.2
C40M3	10	Aggregate-mortar interface	14.9	0.9
		Mortar internal interface	29.8	1.8
	20	Aggregate-mortar interface	23.3	1.5
		Mortar internal interface	46.5	3.0
	30	Aggregate-mortar interface	33.7	2.1
		Mortar internal interface	67.4	4.2
C40M6	10	Aggregate-mortar interface	11.3	0.9
		Mortar internal interface	22.6	1.8
	20	Aggregate-mortar interface	22.2	1.5
		Mortar internal interface	34.4	3.0
	30	Aggregate-mortar interface	29.8	2.1
		Mortar internal interface	59.6	4.2

compression cross-section. Therefore, the strain of the cross-section quotes the experiments reported by Zhou *et al*. [23] for simulation calibration. The uniaxial strength of the C40 concrete used in this research is close to that of the C40M0 concrete used in this paper, and the triaxial compressive strength under the condition of 10MPa confining pressure is also 90MPa. Therefore, the peak strains of the two compression cross-sections under this working condition should be close theoretically ($-\varepsilon_3 = 0.0046$). Compared with the confining pressure condition of 10MPa, the triaxial compression peak strain of C40M0 concrete under the confining pressure conditions of 20MPa and 30MPa increased by 42% and 78%, respectively. According to this law, it can be obtained that the triaxial compression peak strain ($-\varepsilon_3$) of C40M0 concrete under the confining pressure of 20MPa and 30MPa is equal to 0.0064 and 0.0080, respectively.

The material parameters of the C40M0 concrete model are obtained by adjusting the tangential bond strength and fracture energy of the cohesive element by trial and error to make the simulation results coincide with the test result. Since the peak strains of the three types of concrete are close in the triaxial experiment, the effect of confining pressure on fracture energy is much greater than that of the concrete type. Therefore, the fracture energy of the C40M3 and C40M6 models are assumed the same as those of the C40M0 model in triaxial compression. Then, the tangential bond strength is adjusted in order to ensure that the simulation and experimental triaxial peak strength are consistent, thus the material parameters of the C40M3 and C40M6 models are obtained. Ultimately, the material parameters of triaxial compression simulation are shown in Table **6**.

As shown in Figure **16** and Figure **17**, with the increase of confining pressure, the parameters of tangential bond strength and fracture energy of the model are significantly improved. This shows that confining pressure can significantly improve the internal friction strength and deformation capacity of concrete. As shown in Figure **16**, the relationship between the tangential bond strength (T_c) of the mortar internal cohesive element and the confining pressure (f_l) is linearly fitted. The result shows that T_c has a good linear relationship with f_l, and the fitting slopes of C40M0, C40M3, and C40M6 concrete models are 1.92, 1.76, and 1.52, respectively, and the fitting slopes decrease with the increase of microcapsule content. This is similar to our previous experimental research conclusion [18-19], that is, the internal friction coefficient of concrete decreases with the increase of microcapsule content. In addition, as shown in Figure **17**, the fracture energy (G_c) of the mortar internal cohesive element also has a good linear relationship with the confining pressure (f_l). Therefore, the result of this paper can be used to predict the tangential bond strength and fracture energy parameters of the cohesive element model under other confining pressure conditions.

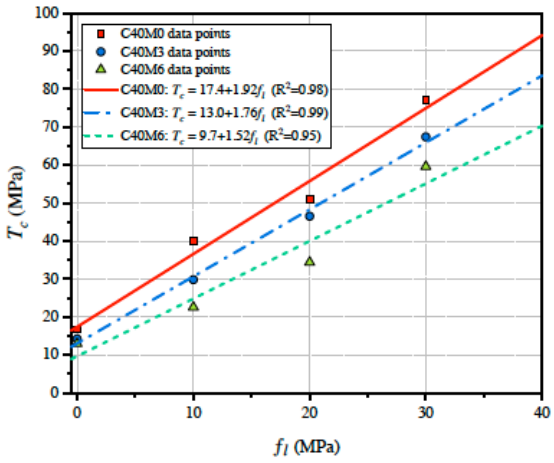

Figure 16: Influence of confining pressure on tangential bond strength (T_c is tangential bond strength of mortar cohesive element).

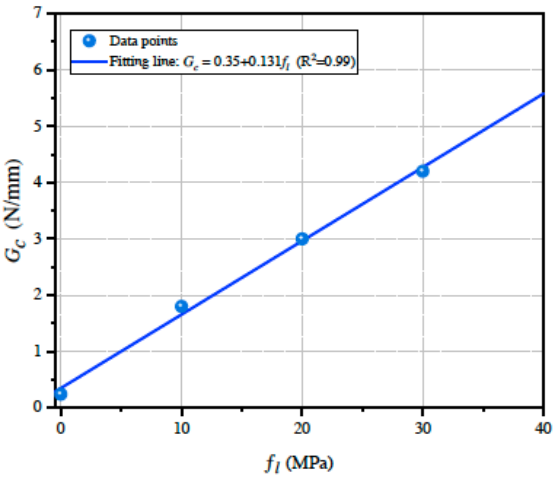

Figure 17: Effect of confining pressure on fracture energy (G_c is the fracture energy of the mortar cohesive element).

3.2.2. Triaxial Compression Simulation Results

The stress-strain curves of the triaxial compression simulation of the model under different confining pressures are shown in Figure **18**. It can be seen that no matter how much the confining pressure is, the three concretes exhibit linear characteristics in the initial stage. The higher the confining pressure, the longer the linear stage of the test curve. After the linear stage, the slope of the ascending stage at low lateral restraint pressure first begins to decrease. These curve characteristics are consistent with the experimental results in this paper. However, regardless of the confining pressure, the post-peak evolution of the simulation curve does not appear as a plateau segment,

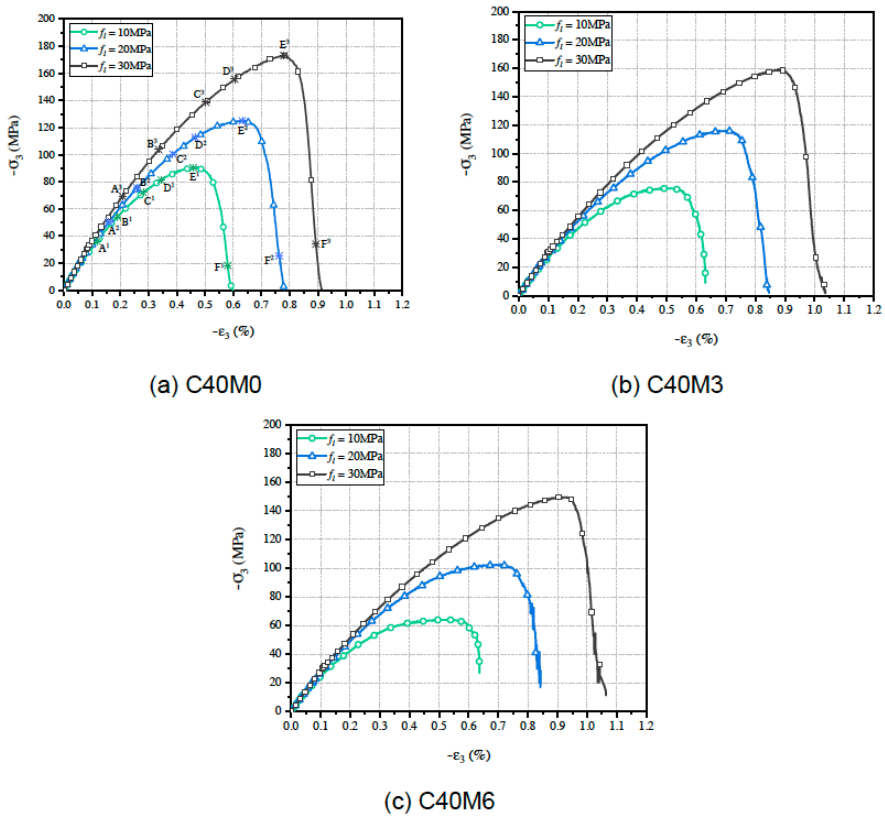

Figure 18: Simulation results of stress-strain curve under triaxial compression.

which is quite different from our experimental result. This is due to the complete loss of bearing capacity of the cohesive element in the model after damage and failure, resulting in rapid failure of the specimen.

The failure modes of the model under triaxial compression simulation under different confining pressures are shown in Figures **19** and Figure **20**. It can be seen that the failure of the model is dominated by an oblique crack accompanied by parallel small cracks. It shows that the model is dominated by "oblique shear" failure, which is consistent with the failure mode of the experiment. The parallel small cracks are caused by the continuous compression of the lateral confining pressure after the "oblique shear" failure of the sample model. The greater the confining pressure, the more parallel small cracks. However, unlike the failure mode of multiple "slant shear" cracks in the experiment, the failure mode of the simulated model is a single "slant shear" crack. This is because the cohesive element of the model completely loses its bearing capacity after being completely damaged, the sample fails completely, and the element that is close to complete damage cannot continue to develop into macroscopic cracks. Furthermore, the failure modes of different types of concrete do not differ substantially.

As shown in Figures **21** to **23**, taking the C40M0 model as an example, the fracture process of the model in the triaxial compression simulation under different confining pressure conditions is illustrated by analyzing the development of the damaged element. In each Figure, (**a**)~(**f**) correspond to Ai~Fi points in different loading stages in Figure **18**, respectively. It can be found by comparing Figure **21**(**a**)~(**c**) and Figure **14**(**a**)~(**c**) that compared with uniaxial

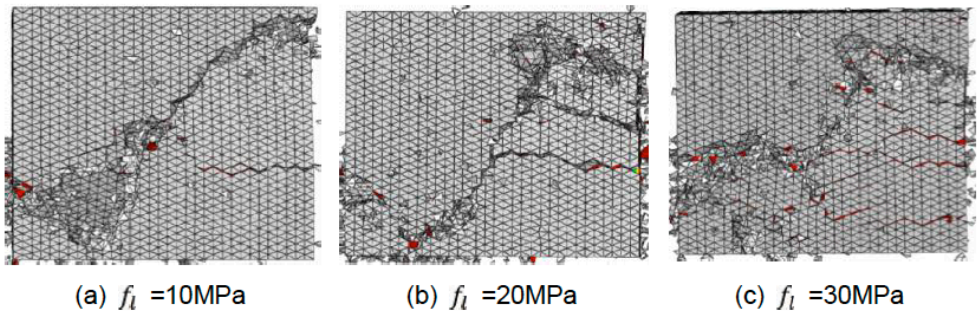

Figure 19: Failure mode of C40M0 model in triaxial compression simulation.

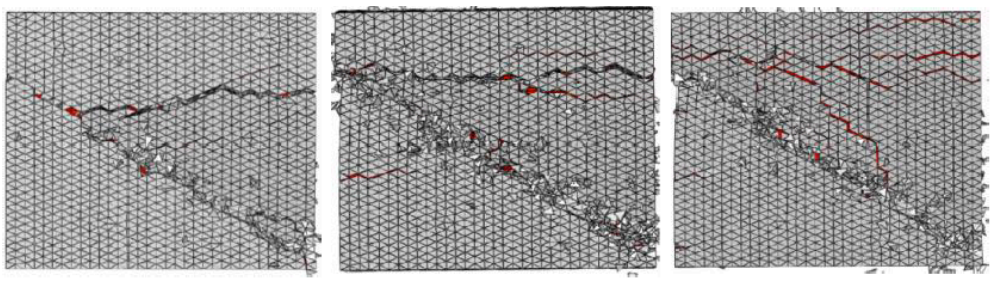

(a) f_l =10MPa (b) f_l =20MPa (c) f_l =30MPa

Figure 20: Failure mode of C40M6 model in triaxial compression simulation.

compression, at the same loading level (for example, $\sigma = 0.4\sigma_{max}$), the model has a significantly more damaged element with D≥0.9. It can also be found by comparing Figure **21**(**a**)~(**c**), Figure **22**(**a**)~(**c**), and Figure **23**(**a**)~(**c**) that under the same loading level (for example, $\sigma = 0.4\sigma_{max}$), the greater the confining pressure of the triaxial compression, the more damaged element (D≥0.9) appear in the model. This shows that under the same loading level, triaxial loading can aggravate the internal damage of the sample, resulting in a large number of microcracks inside the sample. In addition, comparing Figure **21**(**d**)~(**e**) with Figure **14**(**d**)~(**e**), it can be found that the damaged element with D≥0.99 in uniaxial compression only appears in the aggregate-mortar cohesive element. In triaxial compression, this kind of damaged element appears not only in the aggregate-mortar cohesive element but also in the internal cohesive element of mortar. This shows that the cracks of the sample are concentrated in the interfacial transition zone in uniaxial compression, while the cracks of the sample are scattered in the whole sample including the mortar in triaxial compression. It can be found by comparing Figure **21**(**d**)~(**e**), Figure **22**(**d**)~(**e**), and Figure **23**(**d**)~(**e**) that under the same loading level (for example, $\sigma = 0.9\sigma_{max}$), the greater the confining pressure of triaxial compression, the more internal cohesive element of mortar appear damage (D≥0.99) in the model. This shows that under the same loading level, the greater the confining pressure, the more cracks inside the mortar. Finally, it can be observed from Figure **21**(**f**), Figure **22**(**f**), and Figure **23**(**f**) that in the triaxial compression simulation at different confining pressures, the macroscopic cracks (D≥0.999) inside the sample after failure present a three-dimensional shape of "shear plane", which is consistent with the failure mode observed from the surface of the sample.

4. CONCLUSIONS

In this paper, the concrete uniaxial compression and triaxial compression tests are simulated by

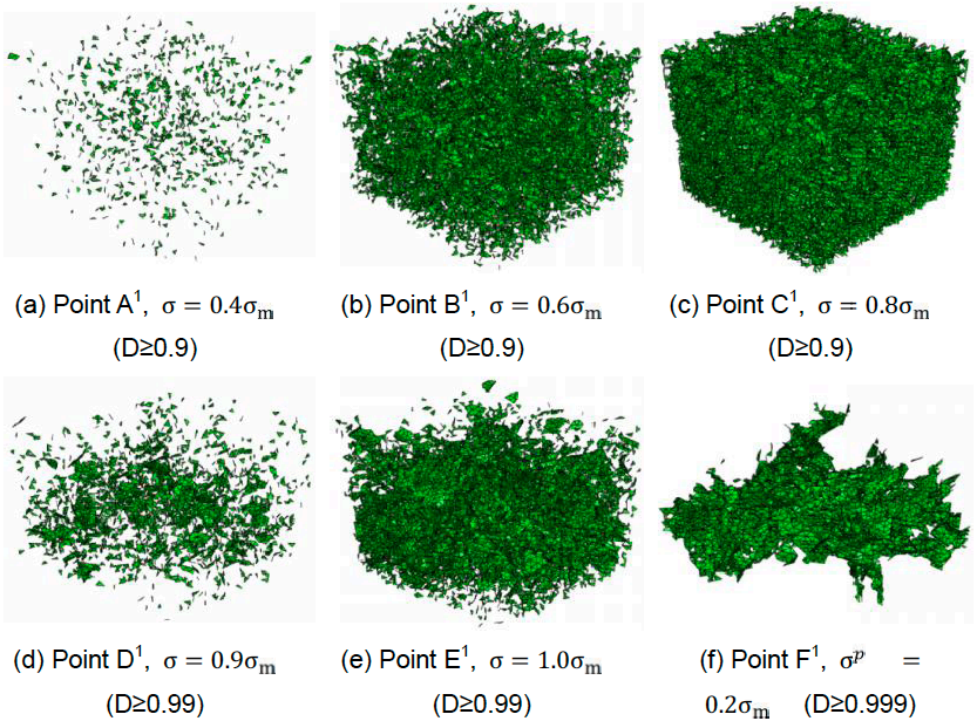

(a) Point A^1, $\sigma = 0.4\sigma_m$ (D≥0.9) (b) Point B^1, $\sigma = 0.6\sigma_m$ (D≥0.9) (c) Point C^1, $\sigma = 0.8\sigma_m$ (D≥0.9)

(d) Point D^1, $\sigma = 0.9\sigma_m$ (D≥0.99) (e) Point E^1, $\sigma = 1.0\sigma_m$ (D≥0.99) (f) Point F^1, $\sigma^p = 0.2\sigma_m$ (D≥0.999)

Figure 21: Fracture process of C40M0 model in triiaxial compression simulation with 10MPa confining pressure.

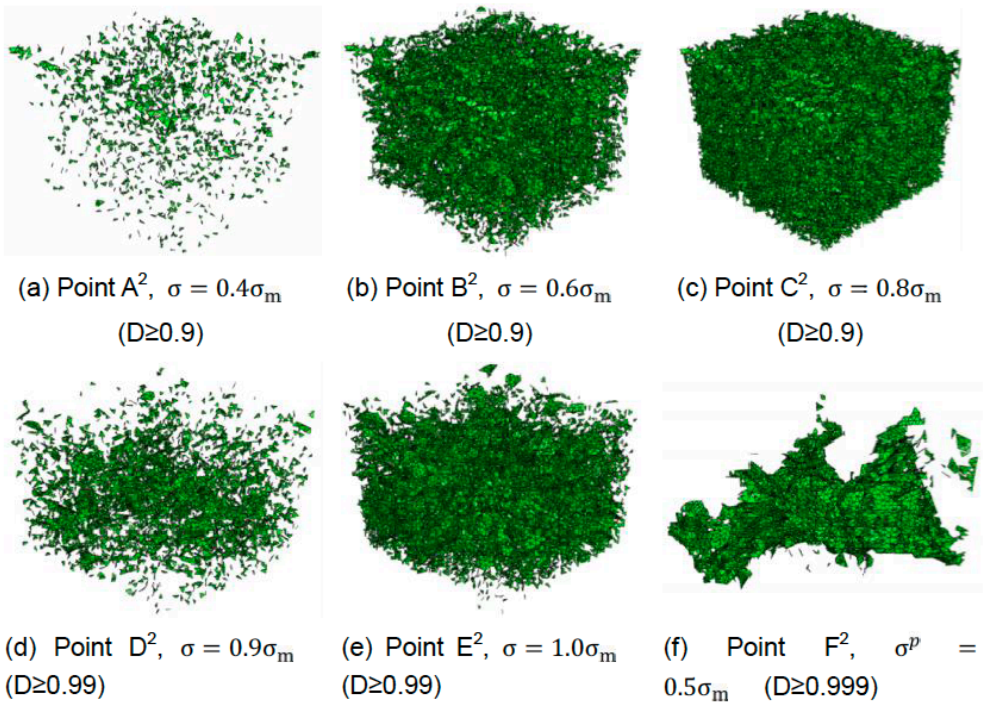

Figure 22: Fracture process of C40M0 model in triaxial compression simulation with 20MPa confining pressure.

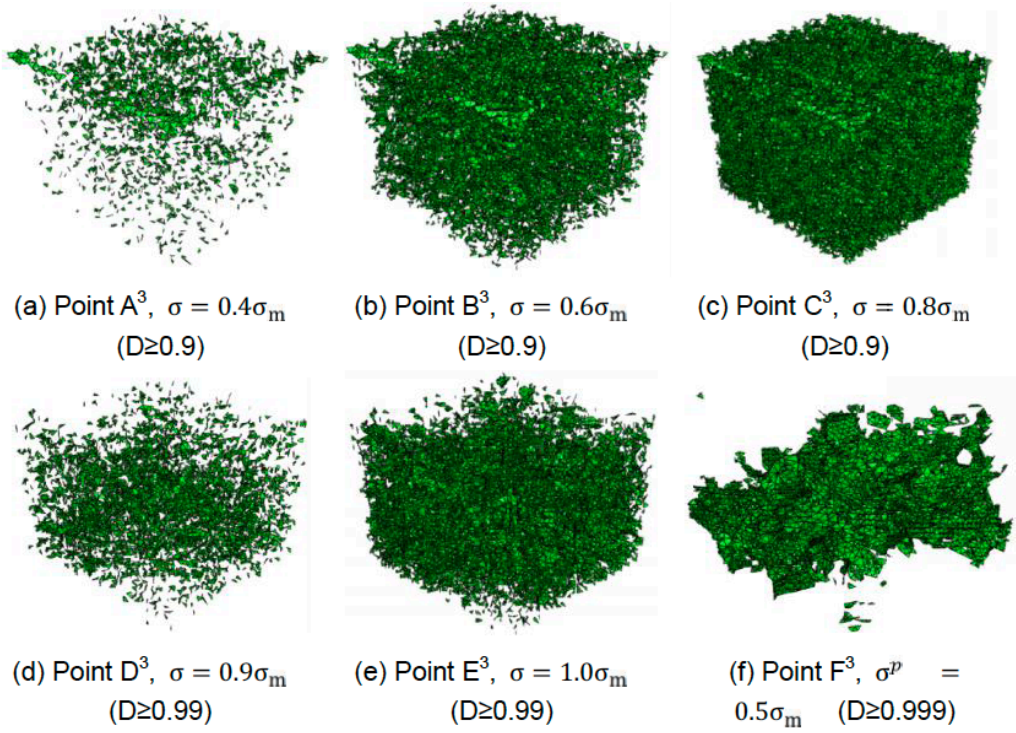

Figure 23: Fracture process of C40M0 model in triiaxial compression simulation with 30MPa confining pressure.

establishing a three-dimensional mesoscopic cohesive crack model of microcapsule self-healing concrete based on the cohesive element that is similar to the actual coarse aggregate gradation. The main conclusions are as follows:

1. In the uniaxial compression simulation, the direction of the softening stage after the peak of the stress-strain curve depends on the relative size relationship between the tangential bond strength parameter and the fracture energy parameter of the cohesive element. That is, the larger the ratio of tangential bond strength to fracture energy, the sharper the curve will drop after the peak, otherwise, the curve will drop slowly after the peak. In addition, the uniaxial strength of the specimen mainly depends on the tangential bond strength. The deformability of

the specimen depends mainly on the fracture energy. The stiffness of the sample depends on the stiffness of the cohesive element and the elastic modulus of the aggregate and mortar element and has nothing to do with the tangential bond strength and fracture energy.

2. The established 3D mesoscopic cohesive crack model of concrete based on the cohesive element can better simulate the failure mode of concrete with different microcapsule content in the uniaxial compression test. The rising stage of the simulated uniaxial compressive stress-strain curve coincides with the experimental results, but the falling stage is quite different from the experimental results. When the uniaxial compression is loaded to $\sigma = 0.4\sigma_{\max}$, a small number of microcracks that cause the nonlinear behavior of the stress-strain curve begin to appear. When the uniaxial compression is loaded near the peak point ($\sigma = 0.9{\sim}1.0\sigma_{\max}$), the internal crack of the sample begins to increase sharply. When the sample fails, multiple macroscopic cracks appear inside the sample and are concentrated in the transition zone of the aggregate-mortar interface.

3. In the triaxial compression simulation, the tangential bond strength parameter (T_c), the fracture energy parameter (G_c), and the confining pressure (f_l) of the cohesive element showed a good linear relationship. The three established models C40M0, C40M3, and C40M6 simulated the specimen failure mode consistent with the "oblique shear" failure mode obtained by the experiment. However, the failure mode is different from the single-crack failure and the multi-crack failure in the experiment. The rising stage of the simulated triaxial compressive stress-strain curve is consistent with the experimental results, but the falling stage is quite different from the experimental results. The difference in the above simulation results is related to the complete loss of bearing capacity after the cohesive element is completely damaged.

4. Under the same loading level, compared with uniaxial compression, the number of damaged elements inside the model increased significantly in the triaxial compression, and the greater the confining pressure, the more damaged element there is. Different from the crack of the sample in uniaxial compression concentrated in the interfacial transition zone, the crack of the sample in triaxial compression is scattered in the interior of the mortar and the interfacial transition zone, and the greater the confining pressure, the more crack in the mortar.

CONFLICT OF INTEREST

No conflict of interest.

AKNOWLEDGEMENTS

The authors gratefully acknowledge the financial support from the National Key R&D Program of China (2022YFE0109300), National Natural Science Foundation of China (51978409), Guangdong Provincial Key Laboratory of Durability for Marine Civil Engineering (2020B1212060074). Shenzhen Science and Technology Research and Development Foundation (20200812110216001).

REFERENCES

[1] Han NX, Xing F. A Comprehensive Review of the Study and Development of Microcapsule Based Self-Resilience Systems for Concrete Structures at Shenzhen University. Materials 2017; 10(1): 2. https://doi.org/10.3390/ma10010002

[2] Luo SQ, Zhao MH, Jiang ZZ, Liu SH, Yang L, Mao YX, Pan CG. Microwave preparation and carbonation properties of low-carbon cement. Construction and Building Materials 2022; 320: 126239. https://doi.org/10.1016/j.conbuildmat.2021.126239

[3] Zhang W, Zheng QF, Ashour A, Han BG. Self-healing cement concrete composites for resilient infrastructures: A review. Composites Part B-Engineering 2020; 189: 107892. https://doi.org/10.1016/j.compositesb.2020.107892

[4] Wang XF, Chen SC, Ren J, Huang RS, Yang ZH, Wang WL, Liu J. Effect of super absorbent polymer and mineral additives on mechanical, shrinkage and healing properties of self-healing lightweight aggregate concrete under different curing regimes. Construction and Building Materials 2022; 357: 129377. https://doi.org/10.1016/j.conbuildmat.2022.129377

[5] Hu LS. Numerical study on cracking process of concrete based on mesoscopic model. Hangzhou: Zhejiang University 2011. (Chinese) https://cdmd.cnki.com.cn/Article/CDMD-10335-1011050150.htm

[6] Caballero A, Lopez CM, Carol I. 3D meso-structural analysis of concrete specimens under uniaxial tension. Computer Methods in Applied Mechanics and Engineering 2006; 195(52): 7182-7195. https://doi.org/10.1016/j.cma.2005.05.052

[7] Elices M, Guinea GV, Gómez J, Planas J. The cohesive zone model: advantages, limitations and challenges. Engineering Fracture Mechanics 2002; 69(2): 137-163. https://doi.org/10.1016/S0013-7944(01)00083-2

[8] Su XT, Yang ZJ, Liu GH. Monte Carlo simulation of complex cohesive fracture in random heterogeneous quasi-brittle materials: A 3D study. International Journal of Solids and Structures 2010; 47(17): 2336-2345. https://doi.org/10.1016/j.ijsolstr.2010.04.031

[9] Zhang XF, Tian Y, Qin P, Xiao TP, Wu Jiang. Mesoscopic simulation research on uniaxial tension of concrete with deformed aggregates based on cohesion model. Hydroelectric Power 2022; 48(05): 73-77. (Chinese) https://www.cnki.com.cn/Article/CJFDTotal-SLFD202205014.htm

[10] Yang ZJ, Huang YJ, Yao F, Liu GH. 3D random mesoscopic concrete discrete fracture simulation based on bonded elements. Engineering Mechanics 2020; 37(08): 158-166.

(Chinese).
http://dx.doi.org/10.6052/j.issn.1000-4750.2019.09.0559

[11] Liu YH. Modeling analysis of asphalt concrete skeleton evolution. Yichang: China Three Gorges University 2022. (Chinese).
https://doi.org/10.27270/d.cnki.gsxau.2022.000304

[12] Deng ZH, Huang HQ, Ye BL, Xiang P. Mechanical Performance of RAC under True-Triaxial Compression after High Temperatures. Journal of Materials in Civil Engineering 2020; 32(8): 04020194.
https://doi.org/10.1061/(ASCE)MT.1943-5533.0003231

[13] Su BY, Zhou ZW, Li ZQ, Wang ZH, Shu XF. Experimental investigation on the mechanical behavior of foamed concrete under uniaxial and triaxial loading. Construction and Building Materials 2019; 209: 41-51.
https://doi.org/10.1016/j.conbuildmat.2019.03.097

[14] Mo Y. Experimental study on size effect of concrete triaxial compression performance and mesoscopic numerical simulation. ChangSha: Hunan University 2019. (Chinese)
https://cdmd.cnki.com.cn/Article/CDMD-10532-1020601676.htm

[15] Wang XF, Yang ZJ, Yates JR, Jivkov AP, Zhang C. Monte Carlo simulations of mesoscale fracture modelling of concrete with random aggregates and pores. Construction and Building Materials 2015; 75: 35-45.
https://doi.org/10.1016/j.conbuildmat.2014.09.069

[16] Liu YP. Simulation of mesoscopic damage and fracture of concrete based on cohesive crack model. Beijing: China Academy of Engineering Physics 2018. (Chinese)
https://cdmd.cnki.com.cn/Article/CDMD-82818-1018070467.htm

[17] Xu DY, Feng BL, Guo JZ. FCM and Fracture Energy of Mode II Fracture of Concrete. Journal of Hohai University, 1990, (03): 8-14. (Chinese)
http://www.cqvip.com/qk/91502x/19903/276664.html

[18] Wang XF, Liang JR, Ren J, Wang WL, Liu J, Xing F. Performance of microcapsule-based self-healing concrete under multiaxial compression with large axial strain: Mechanical properties failure mode, and pore structure. Construction and Building Materials 2022; 350: 128866.
https://doi.org/10.1016/j.conbuildmat.2022.128866

[19] Wang XF, Liang JR, Ren J, Wang WL, Liu J, Xing F. Constitutive relations, mechanical behaviour, and failure criterion of microcapsule-based self-healing concrete under uniaxial and triaxial compression. Journal of Building Engineering 2023; 65: 105773.
https://doi.org/10.1016/j.jobe.2022.105773

[20] Song YP. Constitutive relations and failure criteria of various concrete materials. Beijing: China Water&Power Press 2002. (Chinese)

[21] Xiao J, Long X, Qu WJ, Li L, Jiang HB, Zhong ZC. Influence of sulfuric acid corrosion on concrete stress-strain relationship under uniaxial compression. Measurement 2022; 187: 110318.
https://doi.org/10.1016/j.measurement.2021.110318

[22] Wang GS, Lu DC, Zhou X, Wu YF, Du XL, Xiao Y. A stress-path-independent damage variable for concrete under multiaxial stress conditions. International Journal of Solids and Structures 2020; 206: 59-74.
https://doi.org/10.1016/j.ijsolstr.2020.09.012

[23] Zhou W, Feng P, Lin HW. Constitutive relations of coral aggregate concrete under uniaxial and triaxial compression. Construction and Building Materials 2020; 251: 118957.
https://doi.org/10.1016/j.conbuildmat.2020.118957

Received on 10-04-2023 Accepted on 02-05-2023 Published on 04-05-2023

DOI: https://doi.org/10.31875/2409-9848.2023.10.05